

---

# **Unlocking Potential with Compressive Sensing towards Near Field Antenna Measurement**

**M. Salucci, N. Anselmi, and A. Massa**

2024/05/10

---

## Contents

<b>1</b>	<b>Height of the measurement region <math>H_{\text{meas}} = 3 [\lambda]</math></b>	<b>3</b>
1.0.1	Height of the measurement region $H_{\text{meas}} = 2 [\lambda]$ . . . . .	14
1.0.2	Height of the measurement region $H_{\text{meas}} = 1 [\lambda]$ . . . . .	25
1.0.3	Overall Analysis . . . . .	36

ELEDIA Research Center

# 1 Height of the measurement region $H_{\text{meas}} = 3 [\lambda]$

## Original (OMP) MbD parameters

- Max. number of iterations of the *OMP* algorithm :  $I = \{1; 2; 3; \dots; 10\}$ ;
- Selected iteration to report the results:  $I = 4$ ; this choice is justified by the fact that at this iteration the *OMP* algorithm reaches the best near field error as shown in the following Fig. 1.

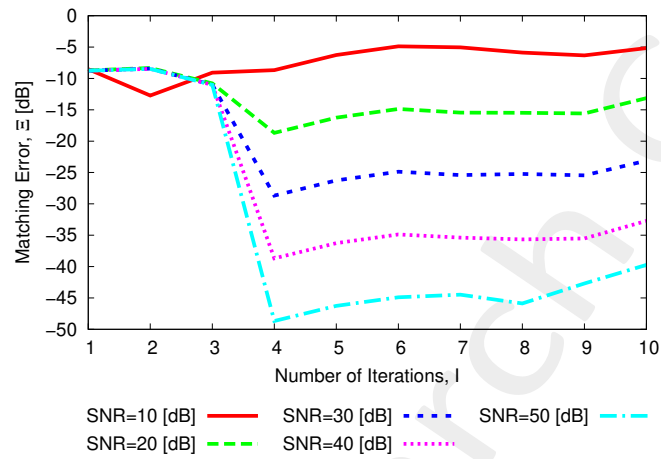


Figure 1: Behaviour of the near-field matching error versus the number of *OMP* iterations,  $I$ .

## Evaluation of the Truncation Error from Actual Near-Field Data

In order to evaluate the truncation error, in the following figure is presented a visual comparison of the near-field radiated by the *AUT* measured over the full interpolation region and on the truncated region, as well as the corresponding far-field patterns obtained with NF-FF transformation. The truncated near-field has been obtained as follows:

$$E_{tr}(\varphi, z) = \begin{cases} E(\varphi, z) & \text{if } -\frac{H_{meas}}{2} \leq z \leq \frac{H_{meas}}{2} \\ 0 & \text{otherwise} \end{cases} ; -\frac{H_{int}}{2} \leq z \leq \frac{H_{int}}{2}$$

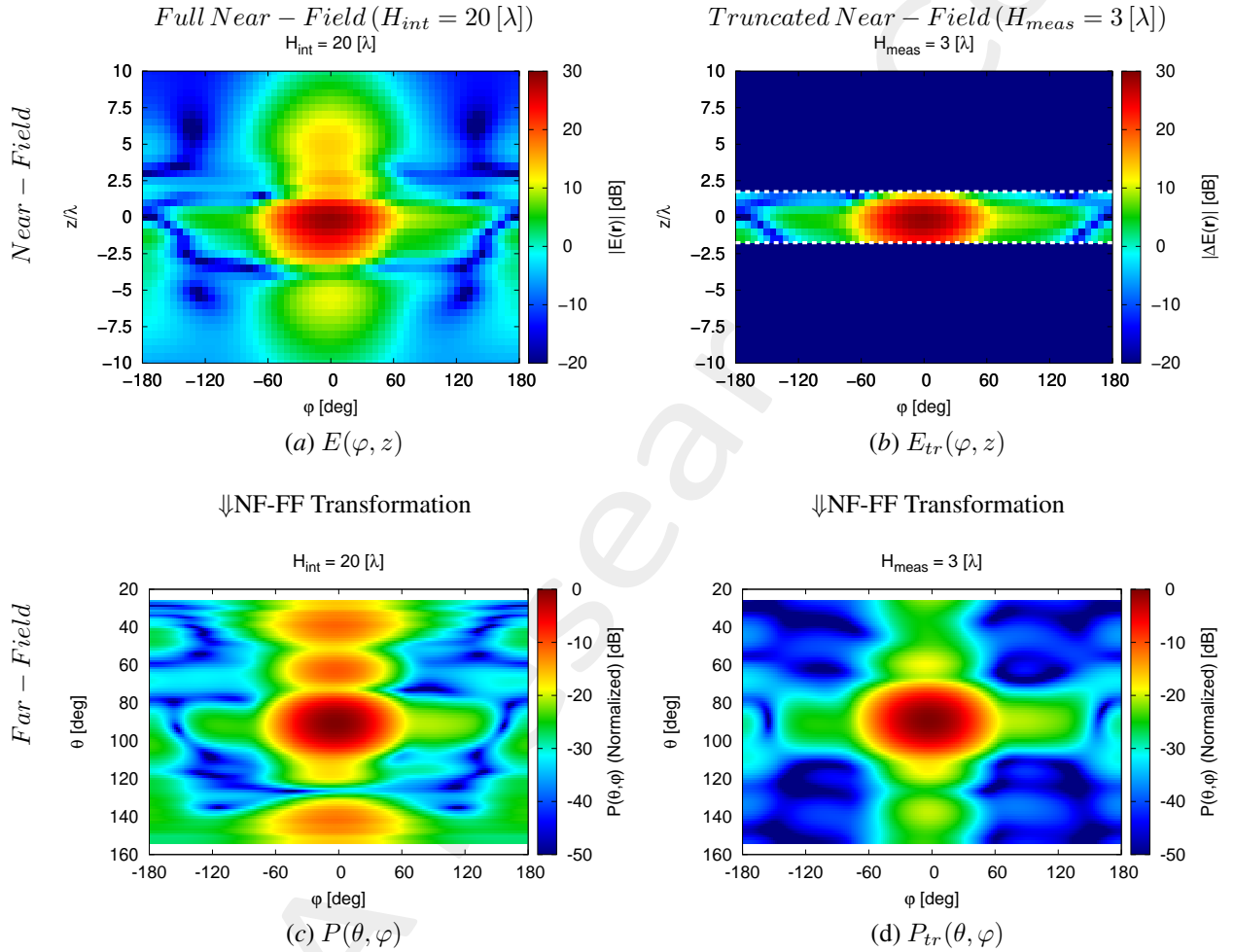


Figure 2:  $H_{meas} = 3 [\lambda]$  - (a)(b) Near-field and (c)(d) far-field patterns obtained via NF-FF transformation for the actual *AUT*.

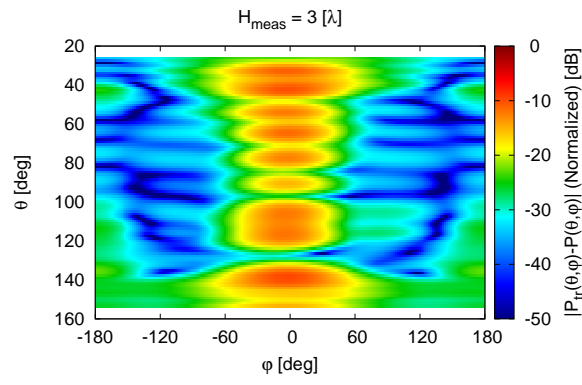


Figure 3:  $H_{meas} = 3 [\lambda]$  - Difference between the full and the truncated far-fields,  $|P(\theta, \varphi) - P_{tr}(\theta, \varphi)|$ .

## Near-Field Error

The comparison, in terms of near field error, between the original (*OMP*) and the alternative (*BCS*) MbD is reported in the following Fig. 4:

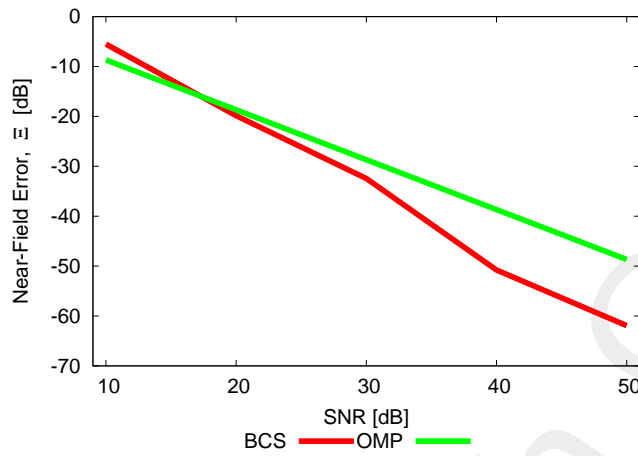


Figure 4: Near Field Error comparison between original (*OMP*) and alternative (*BCS*) MbD for different *SNR* values

<i>SNR</i> [dB]	Near Field Error, $\Xi$ [dB]	
	<i>BCS</i>	<i>OMP</i>
50	-61.93	-48.67
40	-50.78	-38.68
30	-32.44	-28.68
20	-19.85	-18.68
10	-5.49	-8.68

Table I: Near Field Errors obtained by the original (*OMP*) and alternative (*BCS*) MbD

## Observations

By observing the reported results it is possible to point out that :

- the *OMP* error decreases linearly with the increase of the *SNR* reaching good performance ( $\Xi \leq -25$  [dB]) starting from *SNR* = 30 [dB];
- the *BCS* results are not good until *SNR* = 30 [dB] where the *BCS* obtains a result which is better than that of the *OMP* and then the *BCS* continues to improve its performance with the increase of the *SNR* value achieving near-field errors lower than those of the *OMP*.

Estimated Near-Field

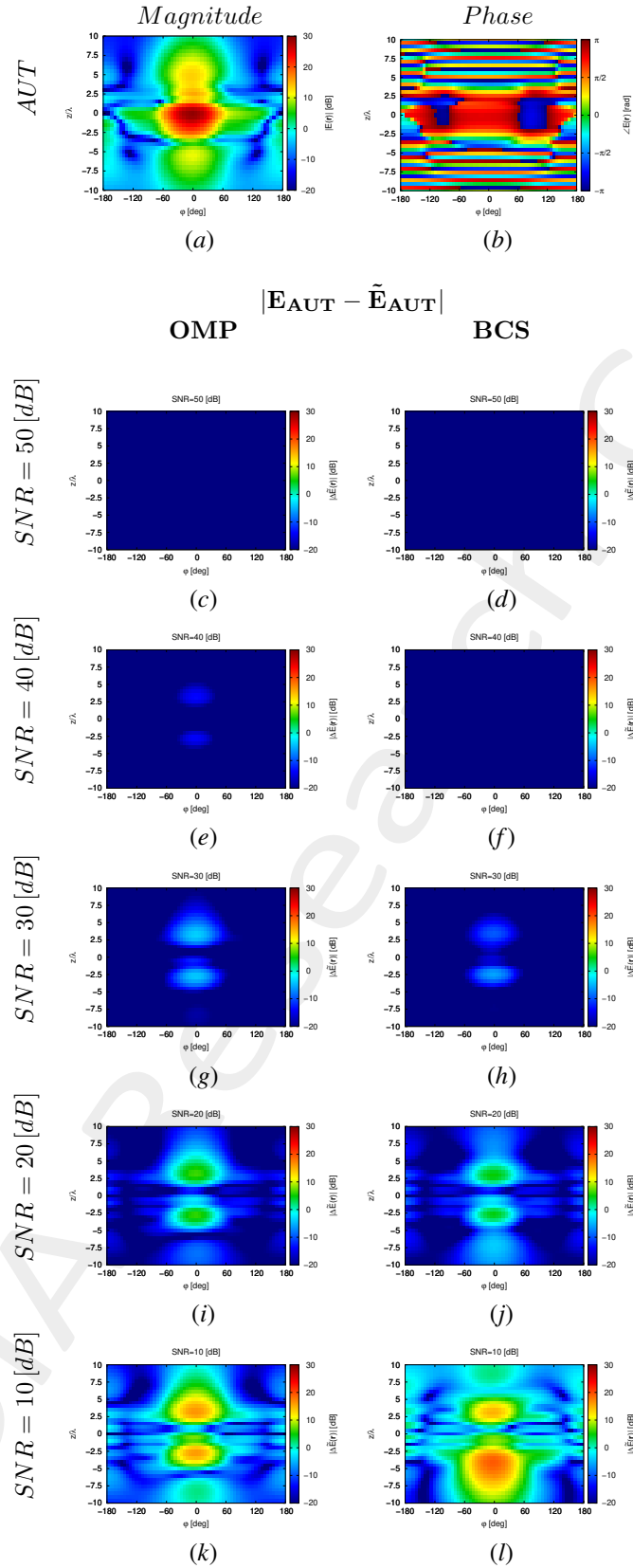


Figure 5: Magnitude difference between the actual and estimated 2 – D near-field pattern when processing noisy measurements at different SNRs.

Estimated Far-Field

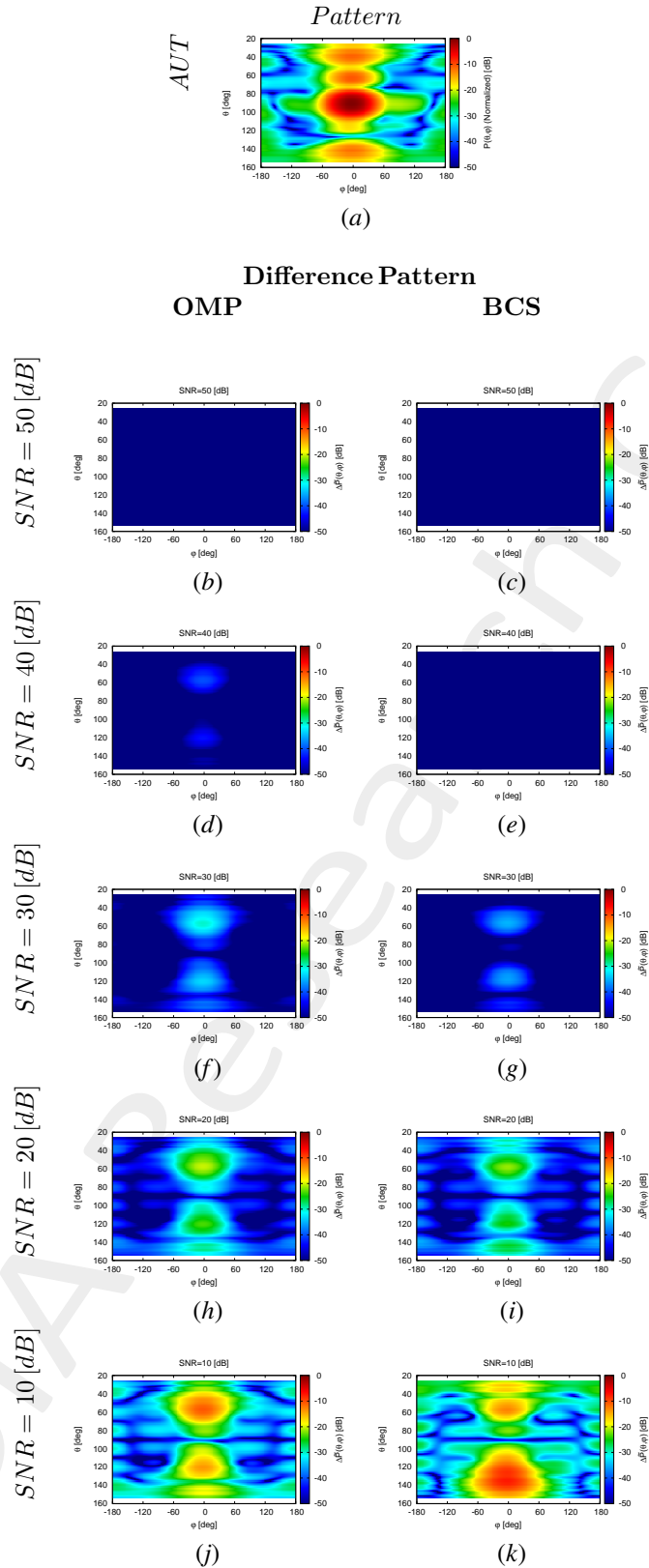


Figure 6: Difference between the actual and estimated 2 –  $D$  far-field pattern when processing noisy measurements at different  $SNRs$ .



Cut @  $\theta = 90$  [deg]

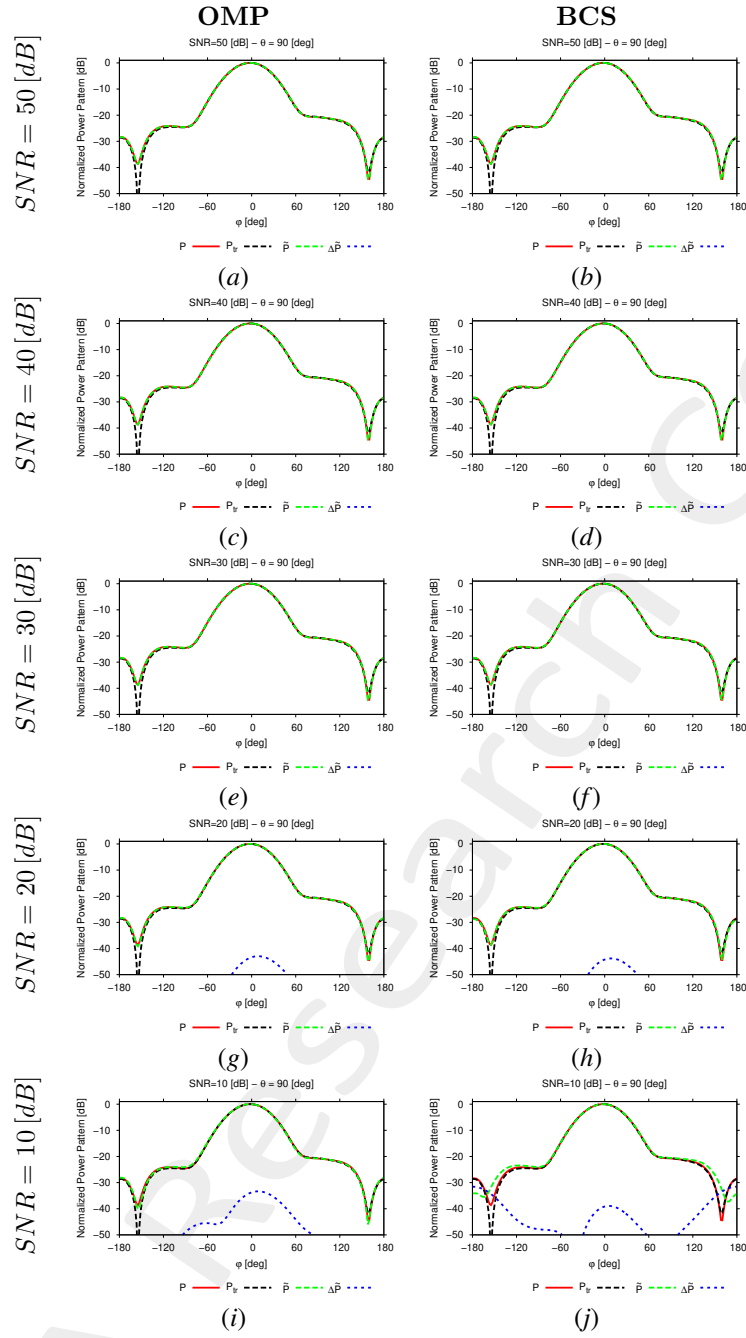


Figure 7: 1-D cuts of the estimated far-field pattern (obtained through near-to-far-field transformation from the estimated near-field patterns) under several noisy conditions

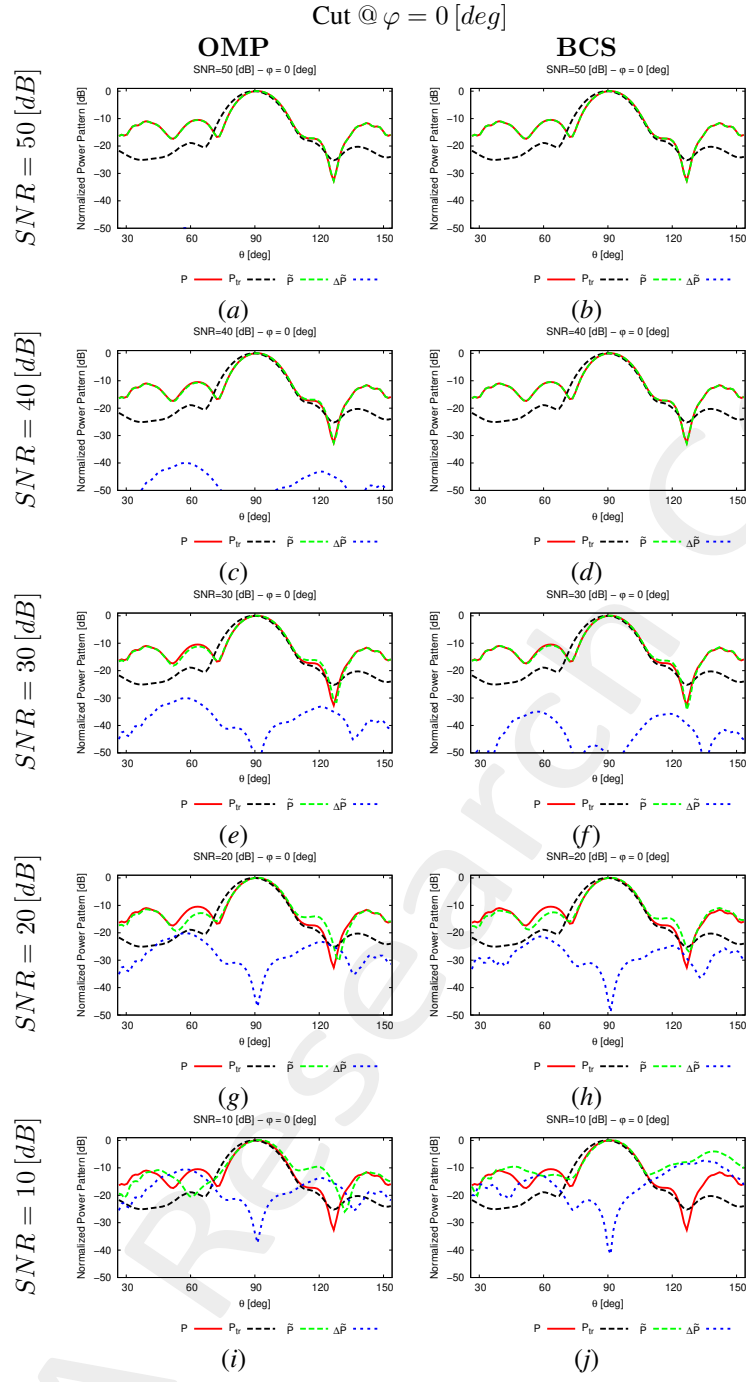


Figure 8: 1-D cuts of the estimated far-field pattern (obtained through near-to-far-field transformation from the estimated near-field patterns) under several noisy conditions

$SNR$ [dB]	Far - Field Error, $\chi$ [dB]	
	BCS	OMP
50	-63.97	-46.32
40	-53.92	-36.34
30	-31.01	-26.39
20	-17.19	-16.52
10	-2.64	-6.93

Table II: Far-field matching error between the actual and estimated  $AUT$  patterns (both obtained through near-to-far-field transformation from the corresponding near-field patterns) under several noisy conditions.

## Estimated Coefficients

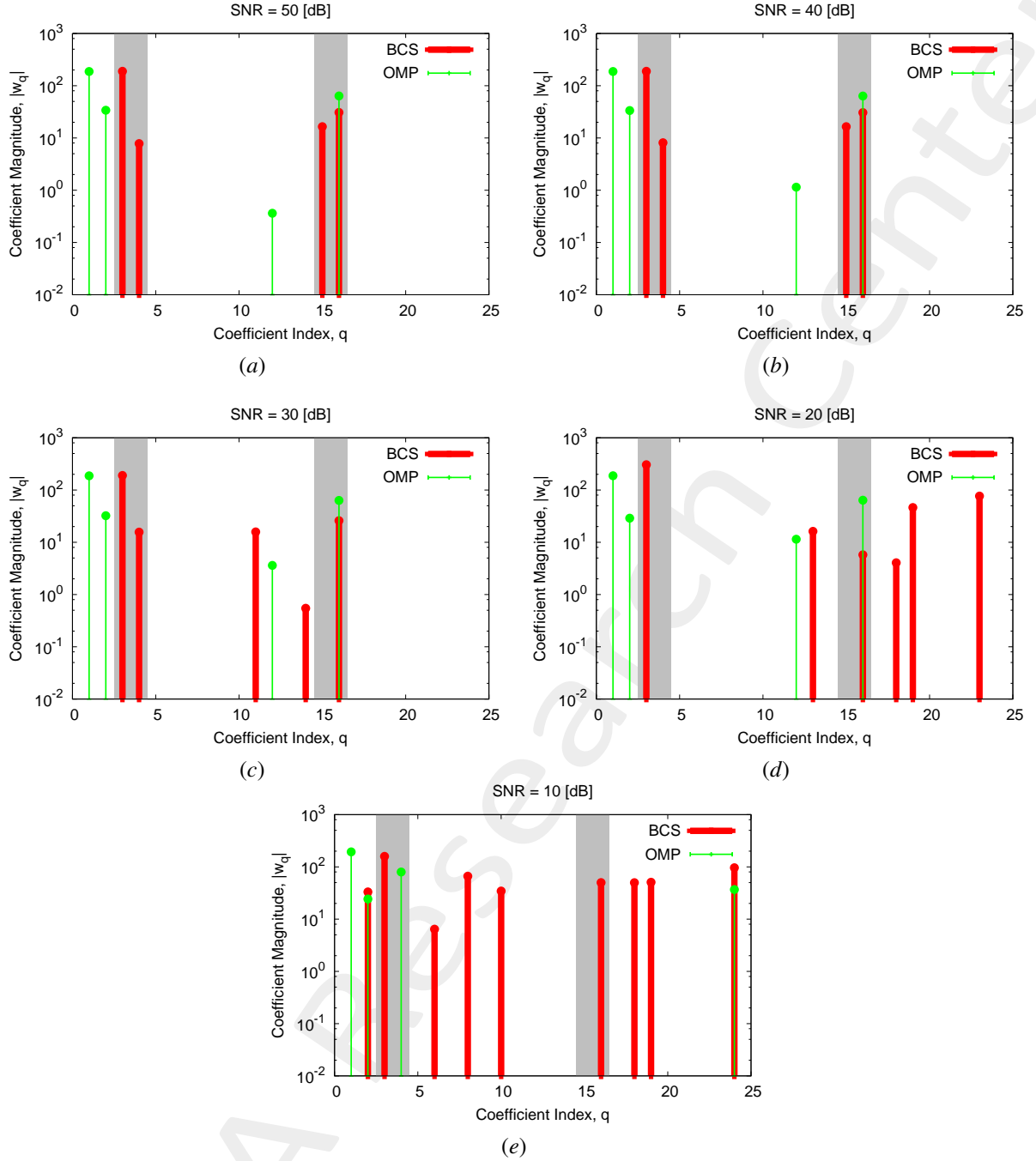


Figure 9: Coefficient comparison between original (*OMP*) and alternative (*BCS*) MbD : (a)  $SNR = 50$  [dB], (b)  $SNR = 40$  [dB], (c)  $SNR = 30$  [dB], (d)  $SNR = 20$  [dB], (e)  $SNR = 10$  [dB]

## Observations

The considered *AUT* is characterized by an excitation magnitude and phase of the second subarray (i.e.,  $\nu^{(2)} = 0.43$  and  $\gamma^{(2)} = \frac{\pi}{3}$  [rad]):

- the *OMP* solver selects vectors associated to both magnitude and phase failures and is always able to identify at least one failure affecting the *AUT*.
- the *BCS* algorithm is able to identify both the failures affecting the *AUT* even if the failure detections are not precise since the method selects also vectors not connected to the actual failures and it doesn't pick all the vectors

---

of the failures affecting the *AUT*. In particular, the *BCS* precisely identify both the failures affecting the *AUT* only at  $SNR = 40$  [dB].

ELEDIA Research Center

---

## Computational times

- $\Delta t_{Sim}$ : Time required to simulate the  $K$  AUT configurations used to build the  $(T \times K)$  "pattern matrix";
- $\Delta t_{SVD}$ : Time required to perform the  $SVD$  of the  $(T \times K)$  "pattern matrix";
- $\Delta t_{MbE}^{OMP/BCS}$ : (Mean) Time required by the Measurement-by-Example tool to read the  $SVD$  output and perform the estimation of the AUT radiated field.

$\Delta t_{Sim}$ [sec]	$4.72 \times 10^4$
$\Delta t_{SVD}$ [sec]	$1.79 \times 10^2$
$\Delta t_{MbE}^{BCS}$ [sec]	$2.83 \times 10^{-1}$
$\Delta t_{MbE}^{OMP}$ [sec]	$1.81 \times 10^{-3}$

Table III: Computational times

## Remarks

- Given that the number of simulated AUTs is  $K = S \times (F^{(s)} + P^{(s)}) = 84$ , the average per-AUT simulation time is

$$\Delta t_{FEKO} \simeq \frac{\Delta t_{Sim}}{K} = \frac{4.72 \times 10^4}{84} [\text{sec}] = 5.62 \times 10^2 [\text{sec}]$$

---

### 1.0.1 Height of the measurement region $H_{\text{meas}} = 2 [\lambda]$

#### Original (OMP) MbD parameters

- Max. number of iterations of the *OMP* algorithm :  $I = \{1; 2; 3; \dots; 10\}$ ;
- Selected iteration to report the results:  $I = 5$ ; this choice is justified by the fact that at this iteration the *OMP* algorithm reaches the best near field error as shown in the following Fig. 10.

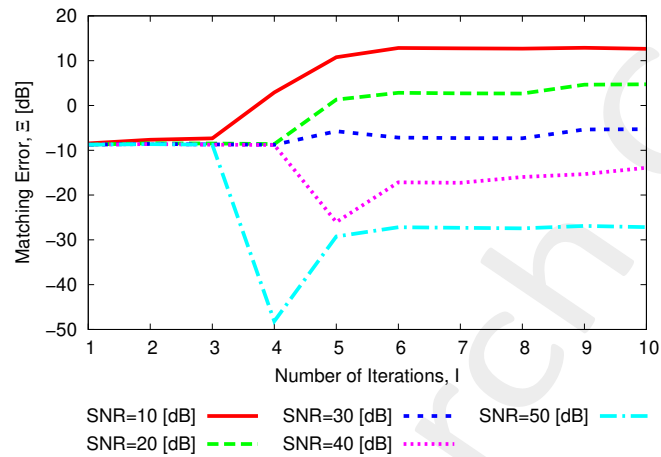


Figure 10: Behaviour of the near-field matching error versus the number of *OMP* iterations,  $I$ .

## Evaluation of the Truncation Error from Actual Near-Field Data

In order to evaluate the truncation error, in the following figure is presented a visual comparison of the near-field radiated by the AUT measured over the full interpolation region and on the truncated region, as well as the corresponding far-field patterns obtained with NF-FF transformation. The truncated near-field has been obtained as follows:

$$E_{tr}(\varphi, z) = \begin{cases} E(\varphi, z) & \text{if } -\frac{H_{meas}}{2} \leq z \leq \frac{H_{meas}}{2} \\ 0 & \text{otherwise} \end{cases} ; -\frac{H_{int}}{2} \leq z \leq \frac{H_{int}}{2}$$

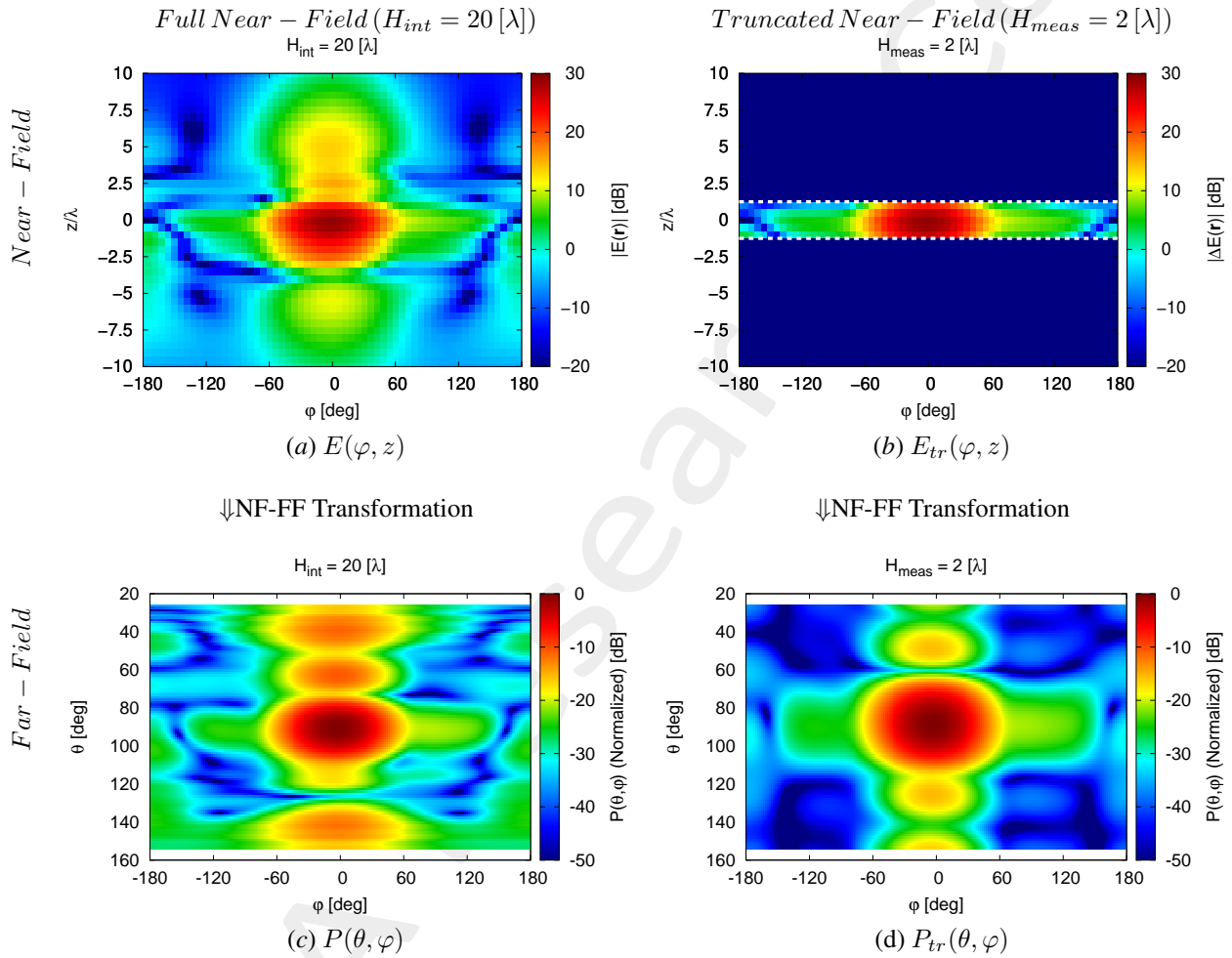


Figure 11:  $H_{meas} = 2 [\lambda]$  - (a)(b) Near-field and (c)(d) far-field patterns obtained via NF-FF transformation for the actual AUT.

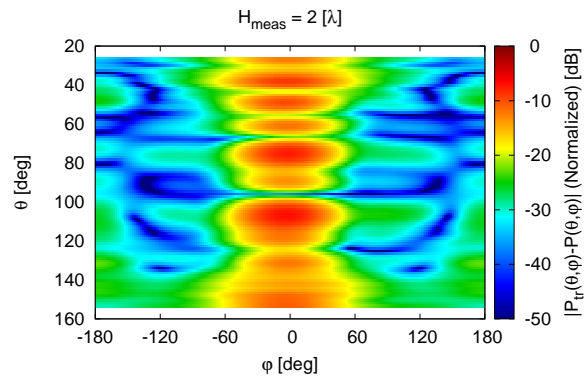


Figure 12:  $H_{meas} = 2 [\lambda]$  - Difference between the full and the truncated far-fields,  $|P(\theta, \varphi) - P_{tr}(\theta, \varphi)|$ .



## Near-Field Error

The comparison, in terms of near field error, between the original (*OMP*) and the alternative (*BCS*) MbD is reported in the following Fig. 13:

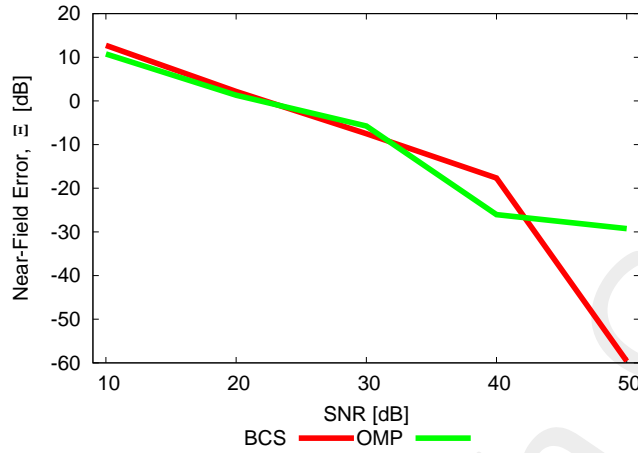


Figure 13: Near Field Error comparison between original (*OMP*) and alternative (*BCS*) MbD for different *SNR* values

<i>SNR</i> [dB]	Near Field Error, $\Xi$ [dB]	
	<i>BCS</i>	<i>OMP</i>
50	-59.59	-29.24
40	-17.65	-26.04
30	-7.51	-5.76
20	2.17	1.32
10	12.74	10.77

Table IV: Near Field Errors obtained by the original (*OMP*) and alternative (*BCS*) MbD

## Observations

By observing the results reported in Fig. 13 it is possible to point out that both the employed algorithms perform poorly with the considered measurement set-up. In particular:

- the *OMP* error is very high at low *SNR* but for  $SNR \geq 40$  [dB] is good enough to permit a good near-field reconstruction;
- the *BCS* algorithm is not able to obtain any satisfactory result until  $SNR = 40$  [dB] since the error does not go below  $-17$  [dB]; however, at  $SNR = 50$  [dB] the *BCS* near-field error is highly better than that of the *OMP* at the same *SNR* value.

Estimated Near-Field

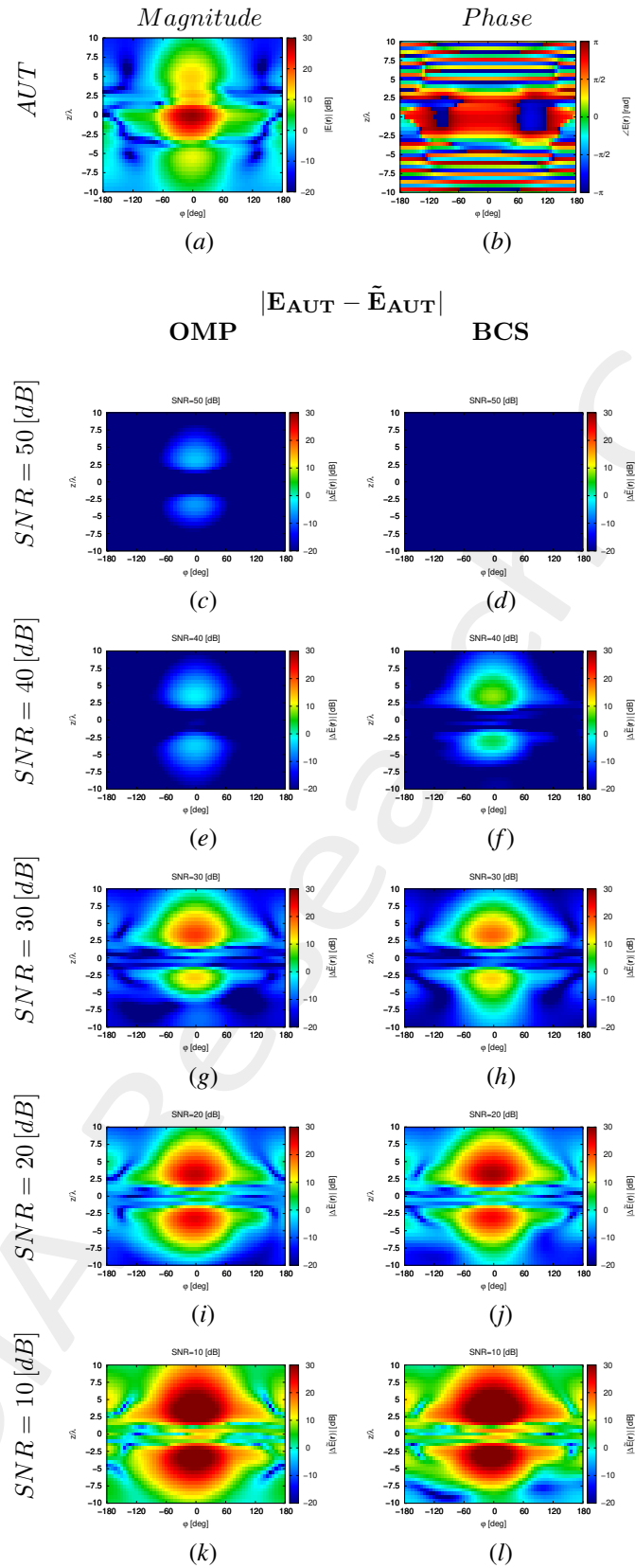


Figure 14: Magnitude difference between the actual and estimated 2 – D near-field pattern when processing noisy measurements at different SNRs.

Estimated Far-Field

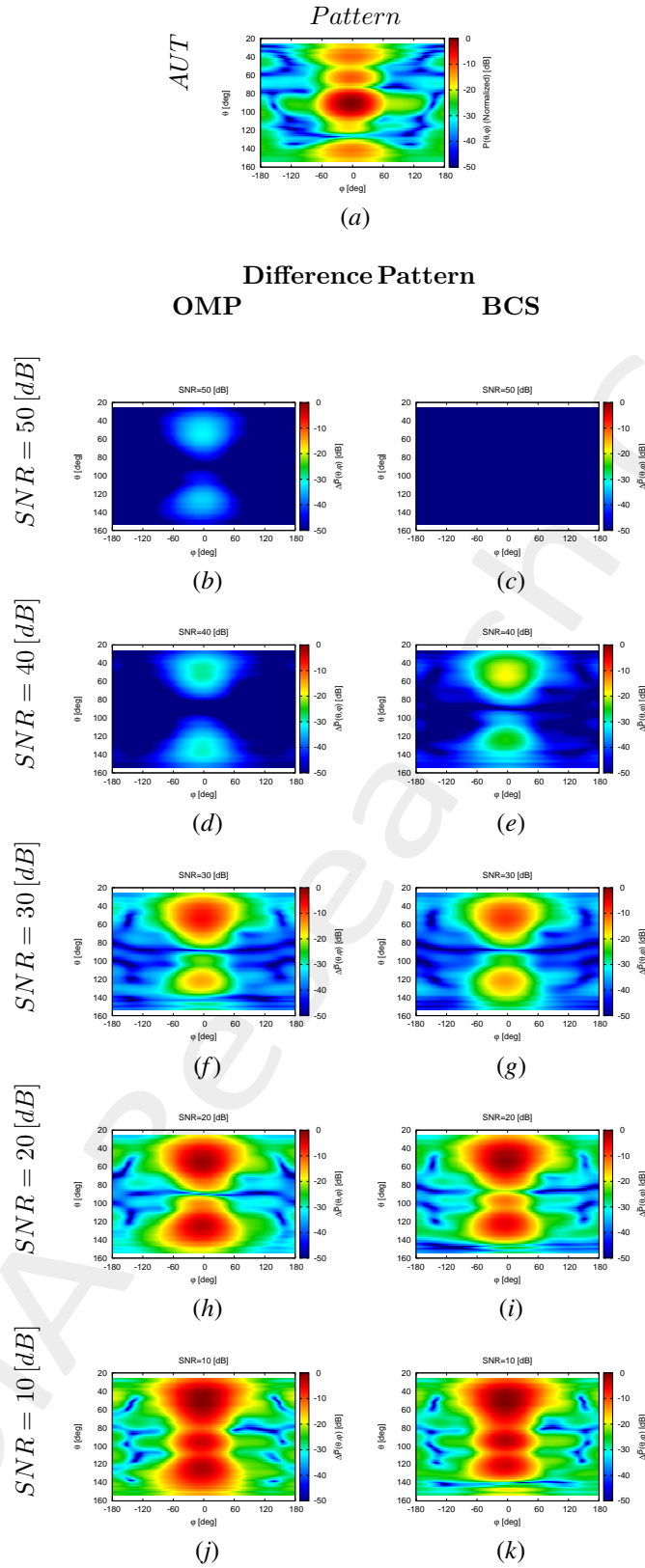


Figure 15: Difference between the actual and estimated 2 –  $D$  far-field pattern when processing noisy measurements at different  $SNRs$ .

Cut @  $\theta = 90$  [deg]

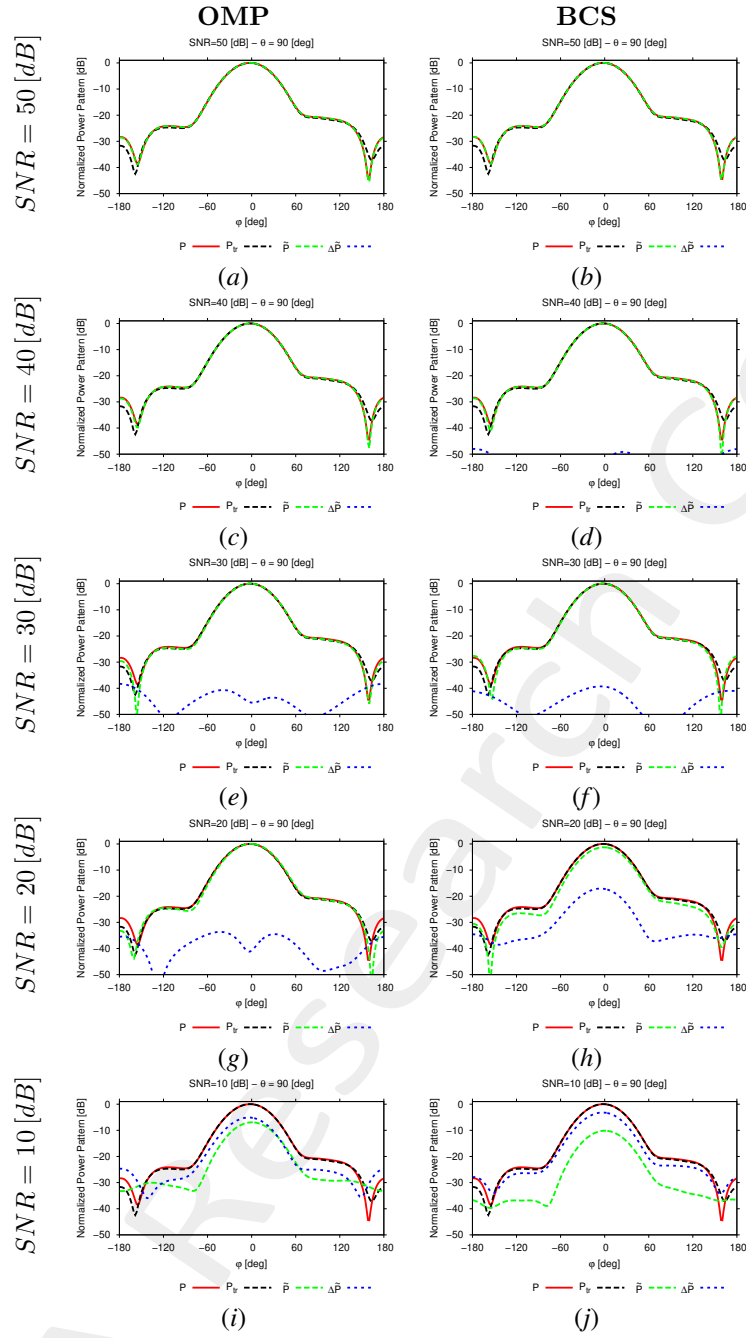


Figure 16: 1 –  $D$  cuts of the estimated far-field pattern (obtained through near-to-far-field transformation from the estimated near-field patterns) under several noisy conditions

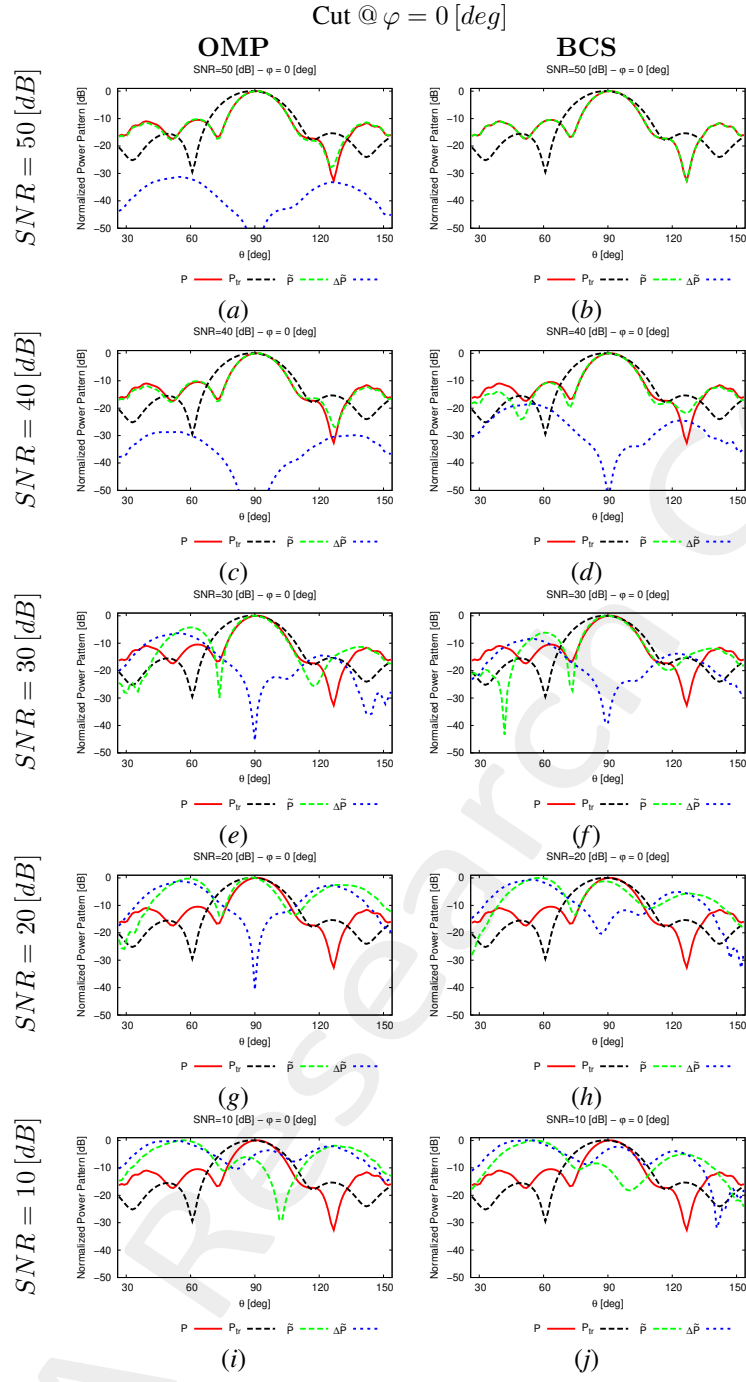


Figure 17: 1 –  $D$  cuts of the estimated far-field pattern (obtained through near-to-far-field transformation from the estimated near-field patterns) under several noisy conditions

$SNR$ [dB]	Far – Field Error, $\chi$ [dB]	
	$BCS$	$OMP$
50	–62.43	–26.27
40	–14.63	–22.07
30	–5.01	–3.24
20	3.03	3.25
10	4.87	5.59

Table V: Far-field matching error between the actual and estimated  $AUT$  patterns (both obtained through near-to-far-field transformation from the corresponding near-field patterns) under several noisy conditions.

## Estimated Coefficients

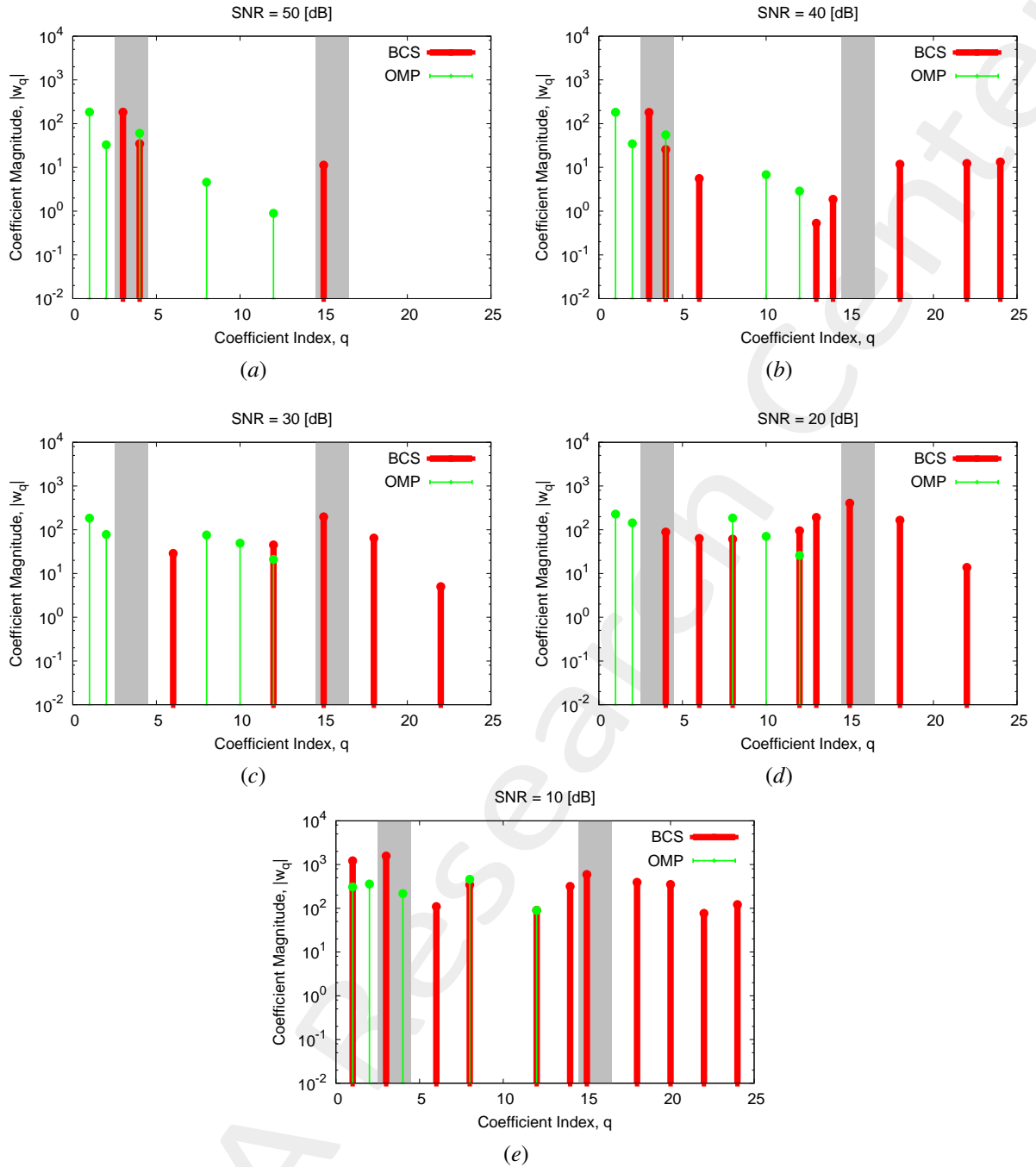


Figure 18: Coefficient comparison between original (*OMP*) and alternative (*BCS*) MbD : (a)  $SNR = 50$  [dB], (b)  $SNR = 40$  [dB], (c)  $SNR = 30$  [dB], (d)  $SNR = 20$  [dB], (e)  $SNR = 10$  [dB]

## Observations

The considered *AUT* is characterized by an excitation magnitude and phase of the second subarray (i.e.,  $\nu^{(2)} = 0.43$  and  $\gamma^{(2)} = \frac{\pi}{3}$  [rad]):

- the *OMP* solver selects vectors associated to both magnitude and phase failures and in some cases is able to identify the magnitude failure affecting the *AUT*.
- the *BCS* algorithm is able to identify at least one failure affecting the *AUT* even if the failure detections are not precise since the method selects also vectors not connected to the actual failures and it doesn't pick all the vectors

---

of the failures affecting the *AUT*. At  $SNR = 50$  [dB] the *BCS* solver precisely identifies both the failures affecting the *AUT*.

ELEDIA Research Center

---

## Computational times

- $\Delta t_{Sim}$ : Time required to simulate the  $K$  AUT configurations used to build the  $(T \times K)$  "pattern matrix";
- $\Delta t_{SVD}$ : Time required to perform the  $SVD$  of the  $(T \times K)$  "pattern matrix";
- $\Delta t_{MbE}^{OMP/BCS}$ : (Mean) Time required by the Measurement-by-Example tool to read the  $SVD$  output and perform the estimation of the AUT radiated field.

$\Delta t_{Sim}$ [sec]	$4.72 \times 10^4$
$\Delta t_{SVD}$ [sec]	$1.79 \times 10^2$
$\Delta t_{MbE}^{BCS}$ [sec]	$2.07 \times 10^{-1}$
$\Delta t_{MbE}^{OMP}$ [sec]	$1.65 \times 10^{-3}$

Table VI: Computational times

## Remarks

- Given that the number of simulated AUTs is  $K = S \times (F^{(s)} + P^{(s)}) = 84$ , the average per-AUT simulation time is

$$\Delta t_{FEKO} \simeq \frac{\Delta t_{Sim}}{K} = \frac{4.72 \times 10^4}{84} [\text{sec}] = 5.62 \times 10^2 [\text{sec}]$$



---

## 1.0.2 Height of the measurement region $H_{\text{meas}} = 1 [\lambda]$

### Original (OMP) MbD parameters

- Max. number of iterations of the OMP algorithm :  $I = \{1; 2; 3; \dots; 10\}$ ;
- Selected iteration to report the results:  $I = 4$ ; this choice is justified by the fact that at this iteration the OMP algorithm reaches the best near field error as shown in the following Fig. 19.

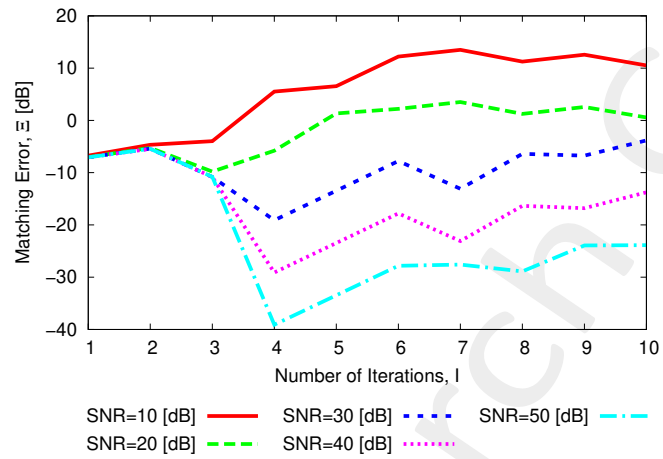


Figure 19: Behaviour of the near-field matching error versus the number of OMP iterations,  $I$ .

## Evaluation of the Truncation Error from Actual Near-Field Data

In order to evaluate the truncation error, in the following figure is presented a visual comparison of the near-field radiated by the *AUT* measured over the full interpolation region and on the truncated region, as well as the corresponding far-field patterns obtained with NF-FF transformation. The truncated near-field has been obtained as follows:

$$E_{tr}(\varphi, z) = \begin{cases} E(\varphi, z) & \text{if } -\frac{H_{meas}}{2} \leq z \leq \frac{H_{meas}}{2} \\ 0 & \text{otherwise} \end{cases} ; -\frac{H_{int}}{2} \leq z \leq \frac{H_{int}}{2}$$

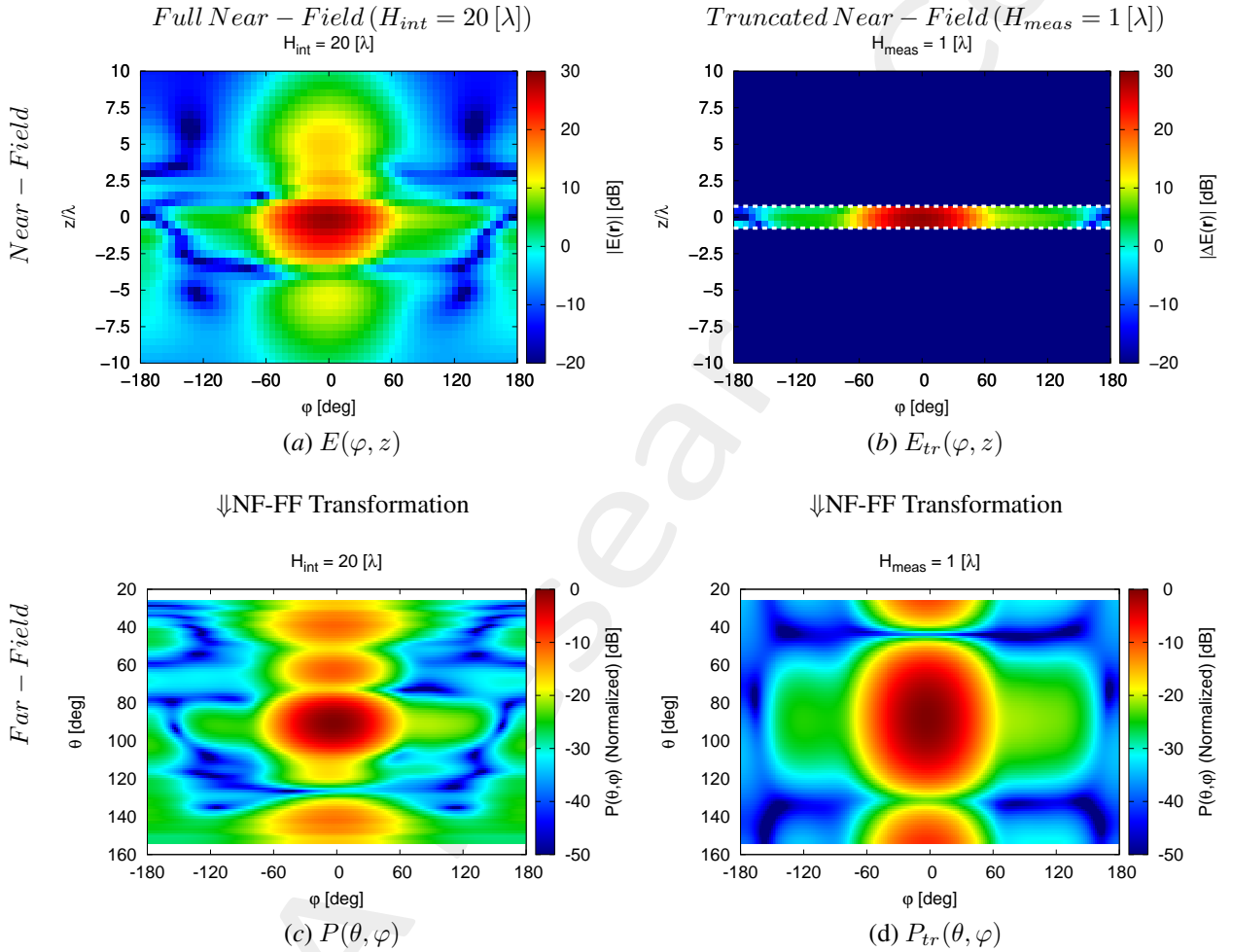


Figure 20:  $H_{meas} = 1 [\lambda]$  - (a)(b) Near-field and (c)(d) far-field patterns obtained via NF-FF transformation for the actual *AUT*.

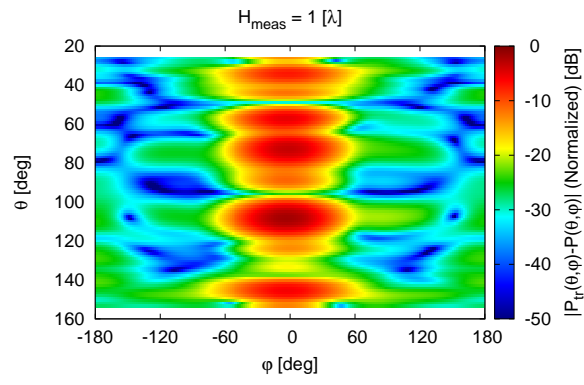


Figure 21:  $H_{meas} = 1 [\lambda]$  - Difference between the full and the truncated far-fields,  $|P(\theta, \varphi) - P_{tr}(\theta, \varphi)|$ .

## Near-Field Error

The comparison, in terms of near field error, between the original (*OMP*) and the alternative (*BCS*) MbD is reported in the following Fig. 22:

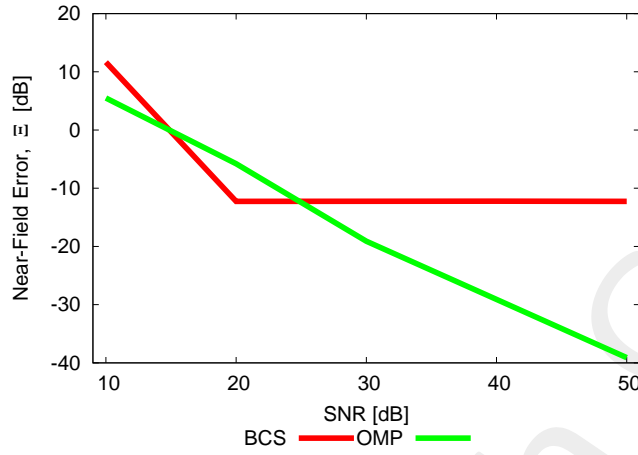


Figure 22: Near Field Error comparison between original (*OMP*) and alternative (*BCS*) MbD for different *SNR* values

<i>SNR</i> [dB]	Near Field Error, $\Xi$ [dB]	
	<i>BCS</i>	<i>OMP</i>
50	-12.26	-39.10
40	-12.22	-29.10
30	-12.23	-19.10
20	-12.26	-5.79
10	11.66	5.51

Table VII: Near Field Errors obtained by the original (*OMP*) and alternative (*BCS*) MbD

## Observations

By observing the results reported in Fig. 22 it is possible to point out that both the employed algorithms perform poorly with the considered measurement set-up. In particular:

- the *OMP* results start to be good for  $SNR \geq 40$  [dB] since for lower *SNR* values the error is  $\Xi > -25$  [dB] which means that the near-field reconstruction is not accurate;
- the *BCS* error remains almost constant at an error value  $\Xi \sim -12$  [dB] which does not permit a good near-field reconstruction.

Estimated Near-Field

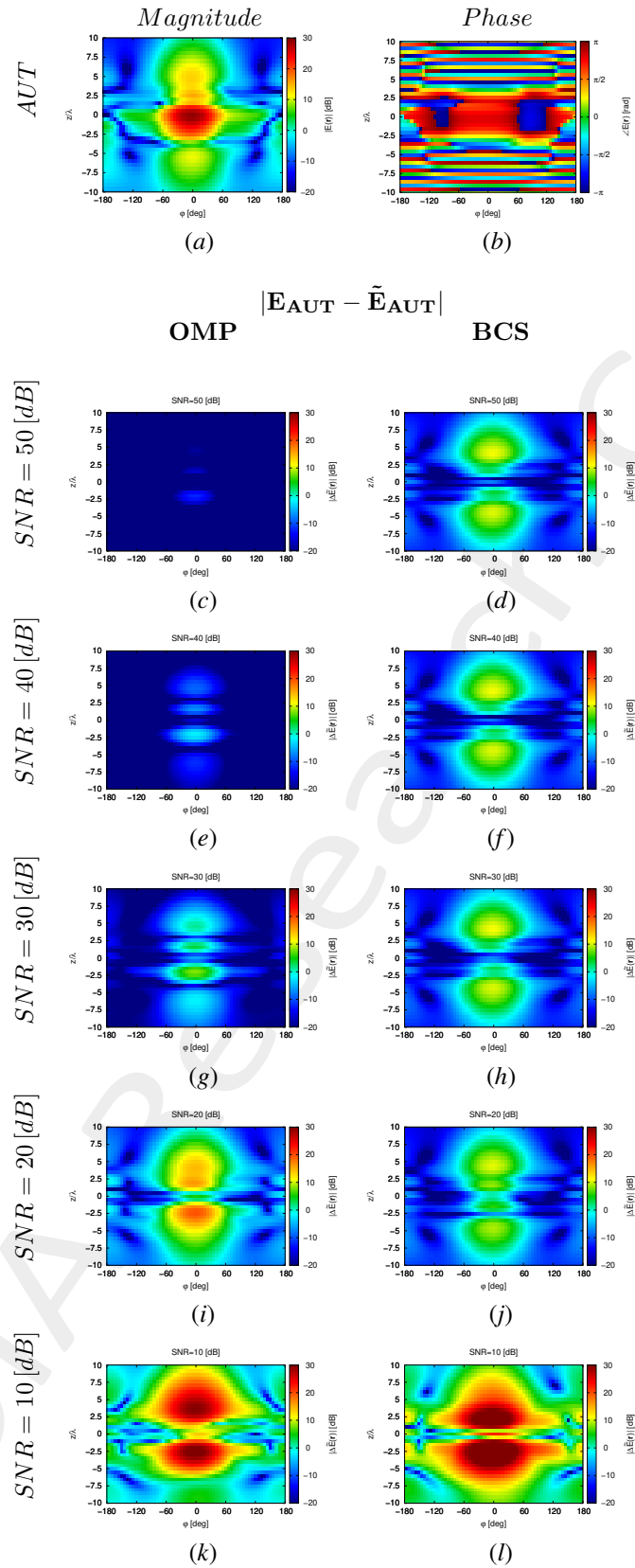


Figure 23: Magnitude difference between the actual and estimated 2 – D near-field pattern when processing noisy measurements at different SNRs.

Estimated Far-Field

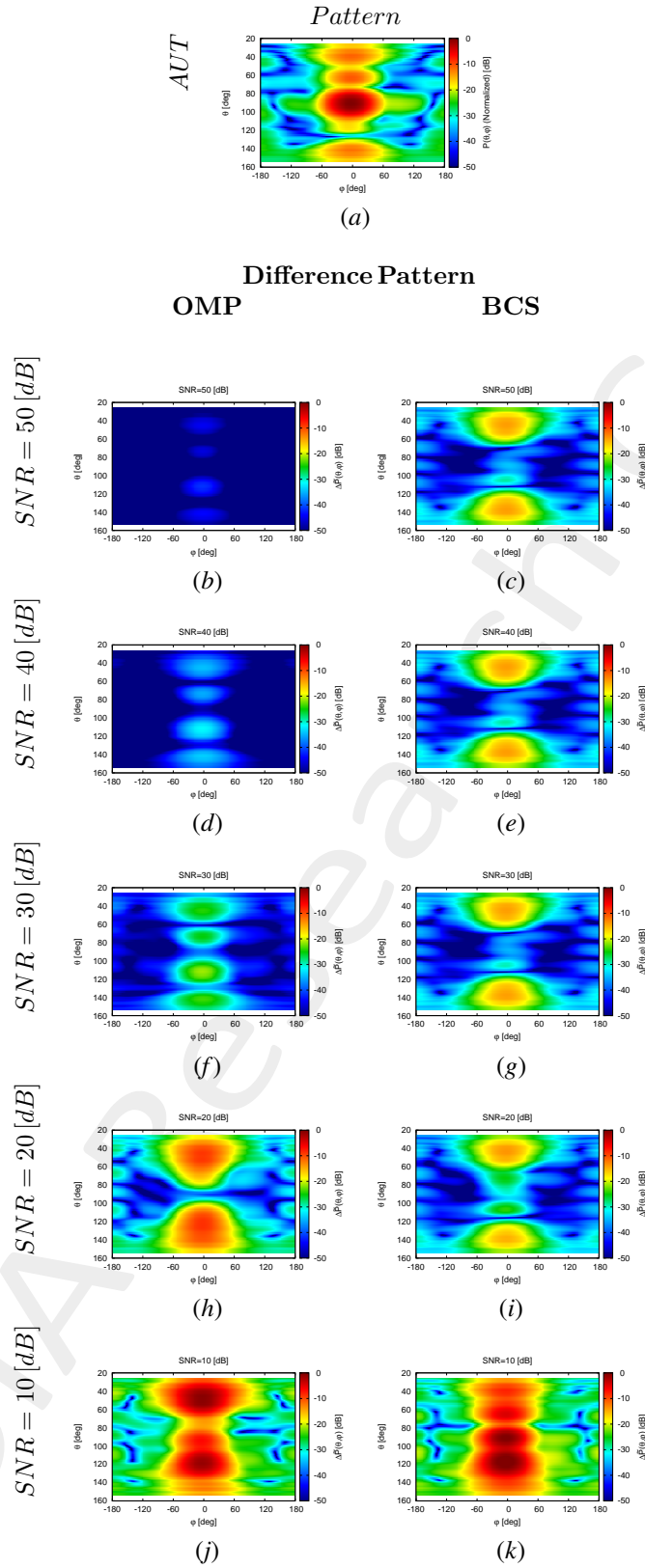


Figure 24: Difference between the actual and estimated 2 – D far-field pattern when processing noisy measurements at different SNRs.

Cut @  $\theta = 90$  [deg]

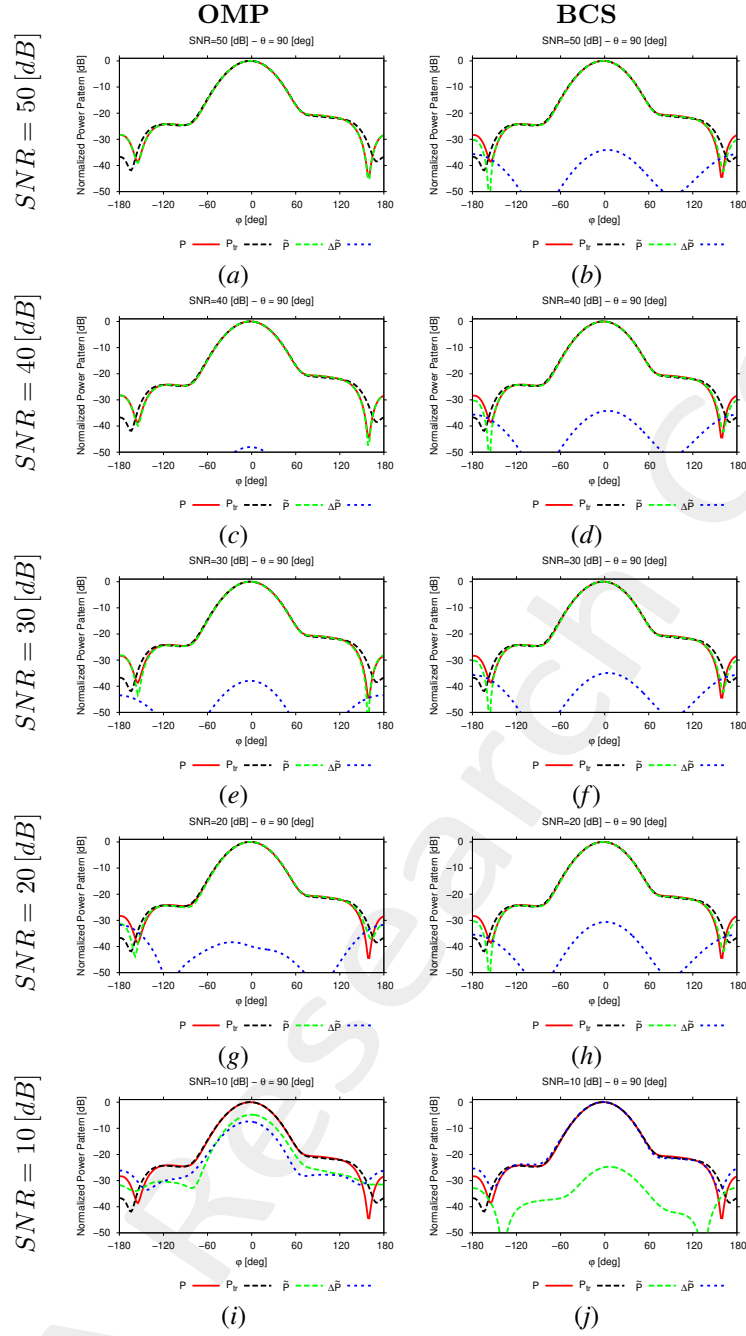


Figure 25: 1 –  $D$  cuts of the estimated far-field pattern (obtained through near-to-far-field transformation from the estimated near-field patterns) under several noisy conditions

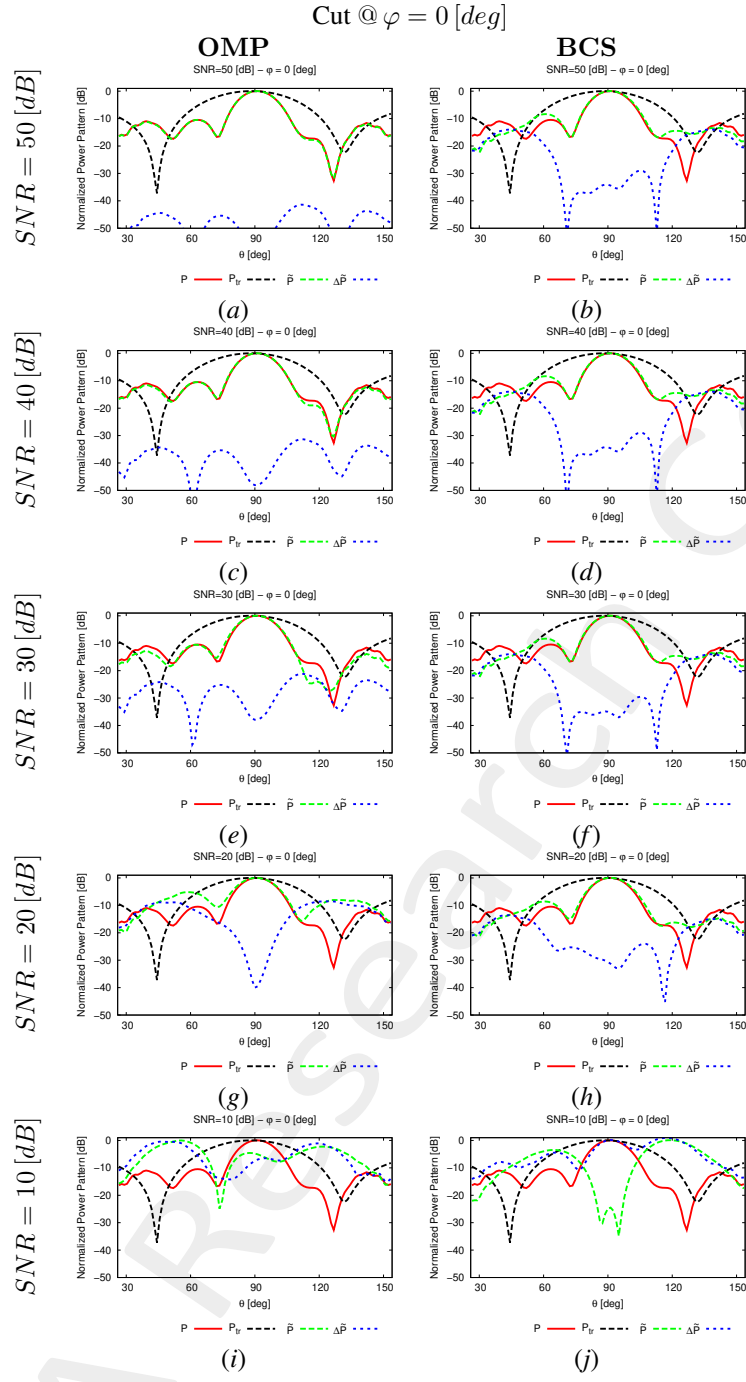


Figure 26: 1 –  $D$  cuts of the estimated far-field pattern (obtained through near-to-far-field transformation from the estimated near-field patterns) under several noisy conditions

$SNR$ [dB]	Far – Field Error, $\chi$ [dB]	
	BCS	OMP
50	-7.11	-36.31
40	-7.11	-26.26
30	-7.15	-16.10
20	-7.26	-1.64
10	4.49	4.87

Table VIII: Far-field matching error between the actual and estimated  $AUT$  patterns (both obtained through near-to-far-field transformation from the corresponding near-field patterns) under several noisy conditions.



## Estimated Coefficients

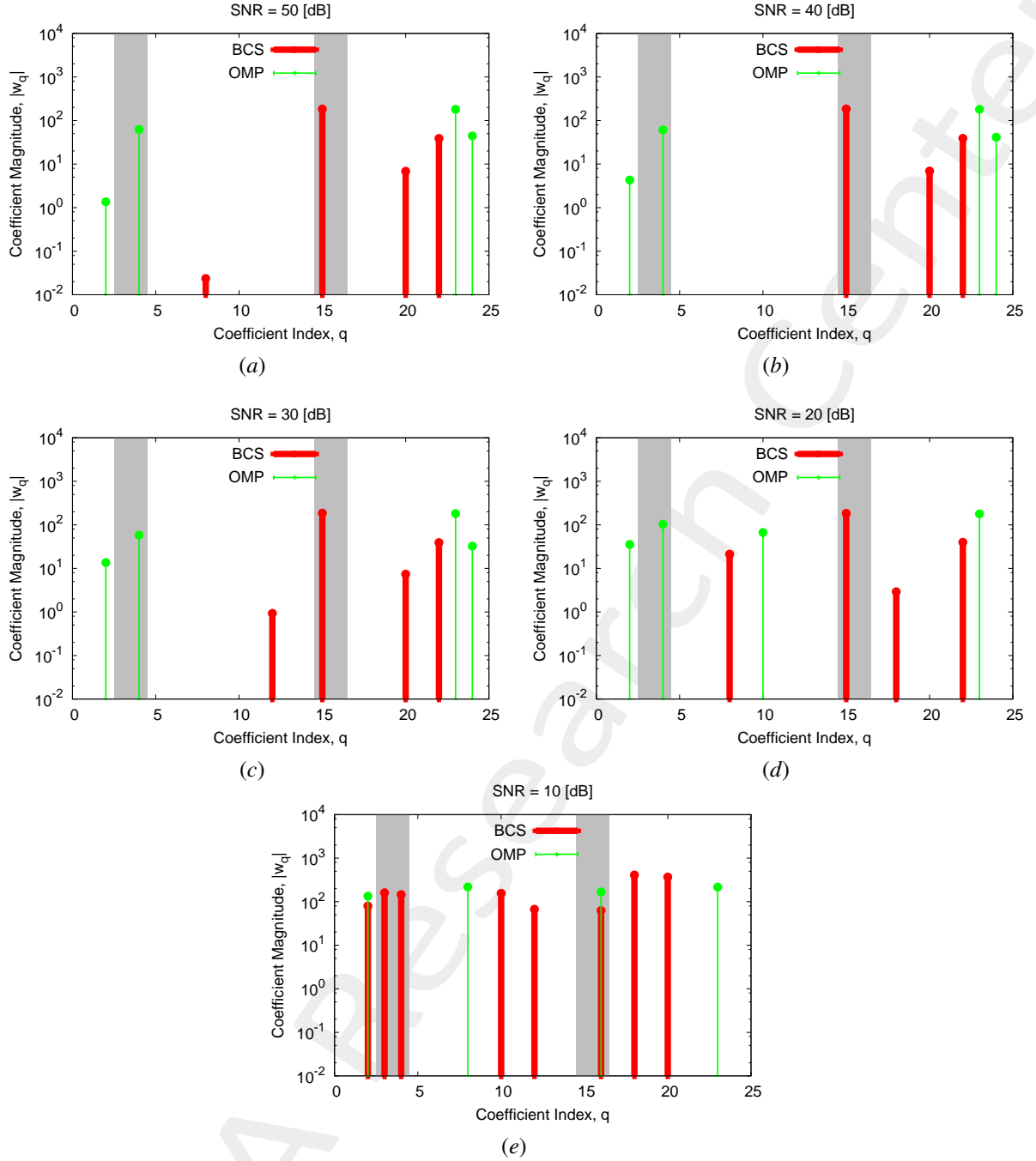


Figure 27: Coefficient comparison between original (*OMP*) and alternative (*BCS*) MbD : (a)  $SNR = 50$  [dB], (b)  $SNR = 40$  [dB], (c)  $SNR = 30$  [dB], (d)  $SNR = 20$  [dB], (e)  $SNR = 10$  [dB]

## Observations

The considered *AUT* is characterized by an excitation magnitude and phase of the second subarray (i.e.,  $\nu^{(2)} = 0.43$  and  $\gamma^{(2)} = \frac{\pi}{3}$  [rad]):

- the *OMP* algorithm is able to identify at least one failure affecting the *AUT* even if the failure detections are not precise since the method selects also vectors not connected to the actual failures and it doesn't pick all the vectors of the failures affecting the *AUT*;
- the *BCS* solver selects vectors associated to both magnitude and phase failures and identifies only the phase failure

---

affecting the *AUT*.

ELEDIA Research Center

---

## Computational times

- $\Delta t_{Sim}$ : Time required to simulate the  $K$  AUT configurations used to build the  $(T \times K)$  "pattern matrix";
- $\Delta t_{SVD}$ : Time required to perform the  $SVD$  of the  $(T \times K)$  "pattern matrix";
- $\Delta t_{MbE}^{OMP/BCS}$ : (Mean) Time required by the Measurement-by-Example tool to read the  $SVD$  output and perform the estimation of the AUT radiated field.

$\Delta t_{Sim}$ [sec]	$4.72 \times 10^4$
$\Delta t_{SVD}$ [sec]	$1.79 \times 10^2$
$\Delta t_{MbE}^{BCS}$ [sec]	$1.95 \times 10^{-1}$
$\Delta t_{MbE}^{OMP}$ [sec]	$1.54 \times 10^{-3}$

Table IX: Computational times

## Remarks

- Given that the number of simulated AUTs is  $K = S \times (F^{(s)} + P^{(s)}) = 84$ , the average per-AUT simulation time is

$$\Delta t_{FEKO} \simeq \frac{\Delta t_{Sim}}{K} = \frac{4.72 \times 10^4}{84} [\text{sec}] = 5.62 \times 10^2 [\text{sec}]$$

### 1.0.3 Overall Analysis

#### Near-Field Error Analysis

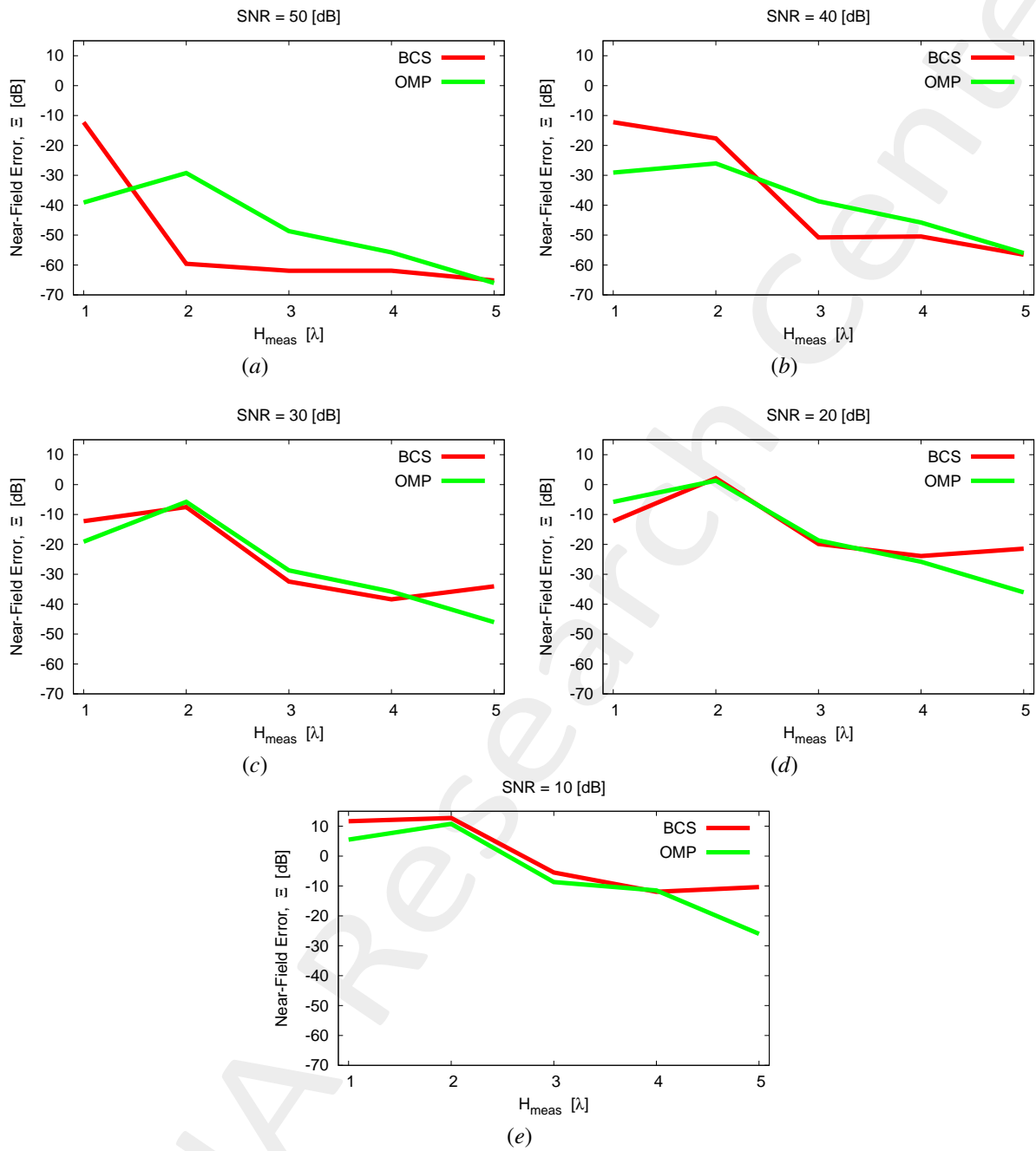


Figure 28: Near-field error vs height of cylindrical set-up at different  $SNR$  values: (a)  $SNR = 50$  [dB], (b)  $SNR = 40$  [dB], (c)  $SNR = 30$  [dB], (d)  $SNR = 20$  [dB], (e)  $SNR = 10$  [dB]

## Far-Field Error Analysis

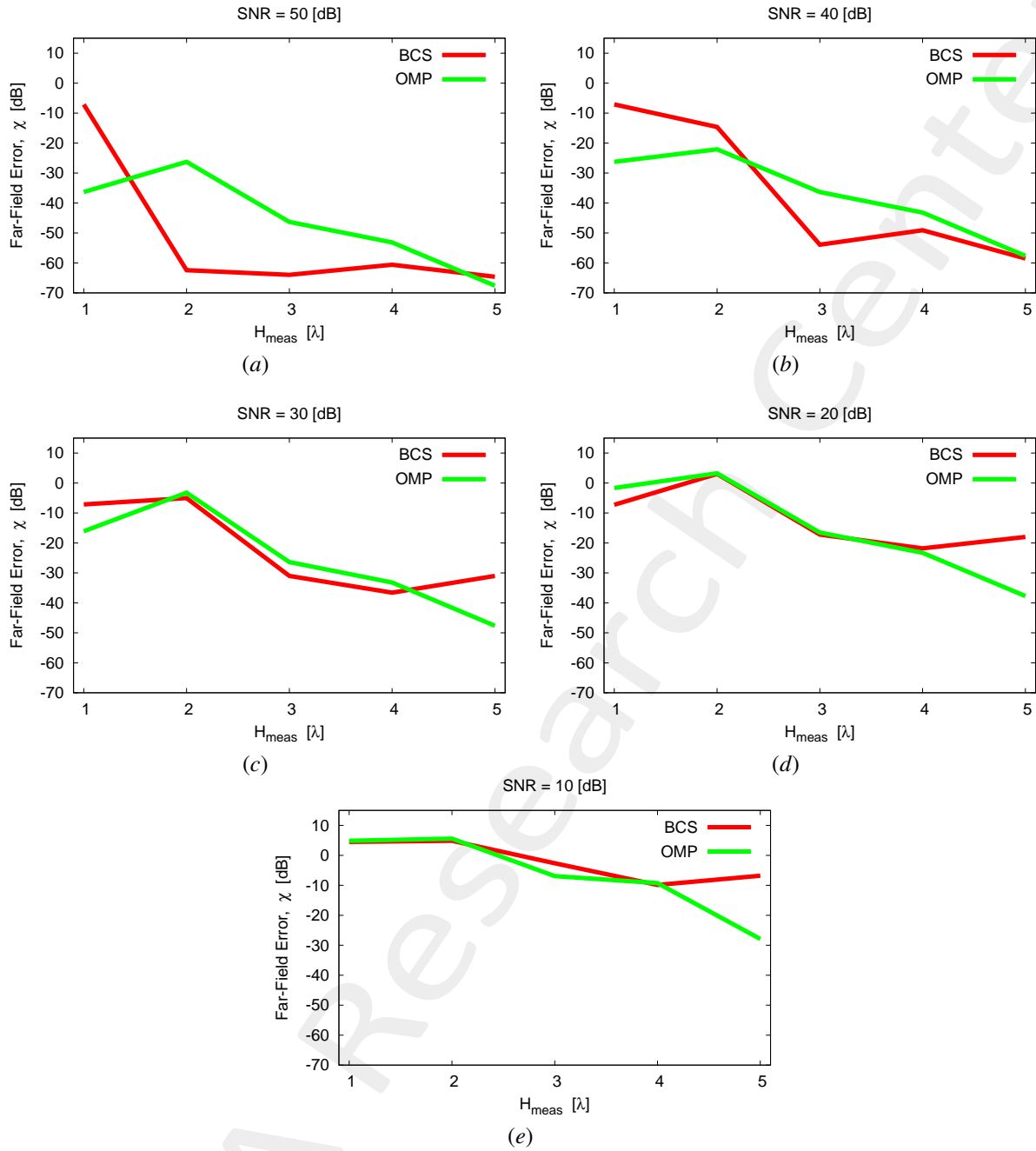


Figure 29: Far-field error vs height of cylindrical set-up at different  $SNR$  values: (a)  $SNR = 50$  [dB], (b)  $SNR = 40$  [dB], (c)  $SNR = 30$  [dB], (d)  $SNR = 20$  [dB], (e)  $SNR = 10$  [dB]

### Observations

In general, from the reported results, it is possible to point out that:

- the  $OMP$  algorithm performs better than the  $BCS$  especially for  $SNR \geq 40$  [dB] where the error gap is noticeable.

---

More information on the topics of this document can be found in the following list of references.

## References

- [1] M. Salucci, N. Anselmi, M. D. Migliore and A. Massa, "A bayesian compressive sensing approach to robust near-field antenna characterization," *IEEE Trans. Antennas Propag.*, vol. 70, no. 9, pp. 8671-8676, Sep. 2022 (DOI: 10.1109/TAP.2022.3177528).
- [2] B. Li, M. Salucci, W. Tang, and P. Rocca, "Reliable field strength prediction through an adaptive total-variation CS technique," *IEEE Antennas Wirel. Propag. Lett.*, vol. 19, no. 9, pp. 1566-1570, Sep. 2020.
- [3] M. Salucci, M. D. Migliore, P. Rocca, A. Polo, and A. Massa, "Reliable antenna measurements in a near-field cylindrical setup with a sparsity promoting approach," *IEEE Trans. Antennas Propag.*, vol. 68, no. 5, pp. 4143-4148, May 2020.
- [4] G. Oliveri, M. Salucci, N. Anselmi, and A. Massa, "Compressive sensing as applied to inverse problems for imaging: theory, applications, current trends, and open challenges," *IEEE Antennas Propag. Mag. - Special Issue on "Electromagnetic Inverse Problems for Sensing and Imaging,"* vol. 59, no. 5, pp. 34-46, Oct. 2017.
- [5] A. Massa, P. Rocca, and G. Oliveri, "Compressive sensing in electromagnetics - A review," *IEEE Antennas Propag. Mag.*, pp. 224-238, vol. 57, no. 1, Feb. 2015.
- [6] A. Massa and F. Teixeira, "Guest-Editorial: Special Cluster on Compressive Sensing as Applied to Electromagnetics," *IEEE Antennas Wirel. Propag. Lett.*, vol. 14, pp. 1022-1026, 2015.
- [7] G. Oliveri, N. Anselmi, M. Salucci, L. Poli, and A. Massa, "Compressive sampling-based scattering data acquisition in microwave imaging," *J. Electromagn. Waves Appl.*, vol. 37, no. 5, pp. 693-729, March 2023 (DOI: 10.1080/09205071.2023.2188263).
- [8] G. Oliveri, L. Poli, N. Anselmi, M. Salucci, and A. Massa, "Compressive sensing-based Born iterative method for tomographic imaging," *IEEE Trans. Microw. Theory Techn.*, vol. 67, no. 5, pp. 1753-1765, May 2019.
- [9] M. Salucci, L. Poli, and G. Oliveri, "Full-vectorial 3D microwave imaging of sparse scatterers through a multi-task Bayesian compressive sensing approach," *J. Imaging*, vol. 5, no. 1, pp. 1-24, Jan. 2019.
- [10] M. Salucci, A. Gelmini, L. Poli, G. Oliveri, and A. Massa, "Progressive compressive sensing for exploiting frequency-diversity in GPR imaging," *J. Electromagn. Waves Appl.*, vol. 32, no. 9, pp. 1164-1193, 2018.
- [11] N. Anselmi, L. Poli, G. Oliveri, and A. Massa, "Iterative multi-resolution bayesian CS for microwave imaging," *IEEE Trans. Antennas Propag.*, vol. 66, no. 7, pp. 3665-3677, Jul. 2018.
- [12] N. Anselmi, G. Oliveri, M. A. Hannan, M. Salucci, and A. Massa, "Color compressive sensing imaging of arbitrary-shaped scatterers," *IEEE Trans. Microw. Theory Techn.*, vol. 65, no. 6, pp. 1986-1999, Jun. 2017.

- 
- [13] N. Anselmi, G. Oliveri, M. Salucci, and A. Massa, "Wavelet-based compressive imaging of sparse targets" *IEEE Trans. Antennas Propag.*, vol. 63, no. 11, pp. 4889-4900, Nov. 2015.
- [14] G. Oliveri, P.-P. Ding, and L. Poli, "3D crack detection in anisotropic layered media through a sparseness-regularized solver," *IEEE Antennas Wirel. Propag. Lett.*, vol. 14, pp. 1031-1034, 2015.
- [15] L. Poli, G. Oliveri, P.-P. Ding, T. Moriyama, and A. Massa, "Multifrequency Bayesian compressive sensing methods for microwave imaging," *J. Opt. Soc. Am. A*, vol. 31, no. 11, pp. 2415-2428, 2014.
- [16] G. Oliveri, N. Anselmi, and A. Massa, "Compressive sensing imaging of non-sparse 2D scatterers by a total-variation approach within the Born approximation," *IEEE Trans. Antennas Propag.*, vol. 62, no. 10, pp. 5157-5170, Oct. 2014.
- [17] L. Poli, G. Oliveri, F. Viani, and A. Massa, "MT-BCS-based microwave imaging approach through minimum-norm current expansion," *IEEE Trans. Antennas Propag.*, vol. 61, no. 9, pp. 4722-4732, Sep. 2013.
- [18] F. Viani, L. Poli, G. Oliveri, F. Robol, and A. Massa, "Sparse scatterers imaging through approximated multitask compressive sensing strategies," *Microwave Opt. Technol. Lett.*, vol. 55, no. 7, pp. 1553-1558, Jul. 2013.
- [19] L. Poli, G. Oliveri, P. Rocca, and A. Massa, "Bayesian compressive sensing approaches for the reconstruction of two-dimensional sparse scatterers under TE illumination," *IEEE Trans. Geosci. Remote Sensing*, vol. 51, no. 5, pp. 2920-2936, May 2013.
- [20] P. Rocca, N. Anselmi, M. A. Hannan, and A. Massa, "Conical frustum multi-beam phased arrays for air traffic control radars," *Sensors*, vol. 22, no. 19, 7309, pp. 1-18, 2022 (DOI: 10.3390/s22197309)
- [21] F. Zardi, G. Oliveri, M. Salucci, and A. Massa, "Minimum-complexity failure correction in linear arrays via compressive processing," *IEEE Trans. Antennas Propag.*, vol. 69, no. 8, pp. 4504-4516, Aug. 2021.
- [22] N. Anselmi, G. Gottardi, G. Oliveri, and A. Massa, "A total-variation sparseness-promoting method for the synthesis of contiguously clustered linear architectures," *IEEE Trans. Antennas Propag.*, vol. 67, no. 7, pp. 4589-4601, Jul. 2019.
- [23] M. Salucci, A. Gelmini, G. Oliveri, and A. Massa, "Planar arrays diagnosis by means of an advanced Bayesian compressive processing," *IEEE Trans. Antennas Propag.*, vol. 66, no. 11, pp. 5892-5906, Nov. 2018.
- [24] L. Poli, G. Oliveri, P. Rocca, M. Salucci, and A. Massa, "Long-Distance WPT Unconventional Arrays Synthesis," *J. Electromagn. Waves Appl.*, vol. 31, no. 14, pp. 1399-1420, Jul. 2017.
- [25] G. Oliveri, M. Salucci, and A. Massa, "Synthesis of modular contiguously clustered linear arrays through a sparseness-regularized solver," *IEEE Trans. Antennas Propag.*, vol. 64, no. 10, pp. 4277-4287, Oct. 2016.
- [26] M. Carlin, G. Oliveri, and A. Massa, "Hybrid BCS-deterministic approach for sparse concentric ring isophoric arrays," *IEEE Trans. Antennas Propag.*, vol. 63, no. 1, pp. 378-383, Jan. 2015.
- [27] G. Oliveri, E. T. Bekele, F. Robol, and A. Massa, "Sparsening conformal arrays through a versatile BCS-based method," *IEEE Trans. Antennas Propag.*, vol. 62, no. 4, pp. 1681-1689, Apr. 2014.
-

- 
- [28] F. Viani, G. Oliveri, and A. Massa, "Compressive sensing pattern matching techniques for synthesizing planar sparse arrays," *IEEE Trans. Antennas Propag.*, vol. 61, no. 9, pp. 4577-4587, Sept. 2013.
- [29] P. Rocca, M. A. Hannan, M. Salucci, and A. Massa, "Single-snapshot DoA estimation in array antennas with mutual coupling through a multi-scaling BCS strategy," *IEEE Trans. Antennas Propag.*, vol. 65, no. 6, pp. 3203-3213, Jun. 2017.
- [30] M. Carlin, P. Rocca, G. Oliveri, F. Viani, and A. Massa, "Directions-of-arrival estimation through Bayesian Compressive Sensing strategies," *IEEE Trans. Antennas Propag.*, vol. 61, no. 7, pp. 3828-3838, Jul. 2013.
- [31] M. Carlin, P. Rocca, G. Oliveri, and A. Massa, "Bayesian compressive sensing as applied to directions-of-arrival estimation in planar arrays," *J. Electromagn. Waves Appl.*, vol. 2013, pp. 1-12, 2013 (DOI :10.1155/2013/245867).